PAPER • OPEN ACCESS

A deep learning and Monte Carlo based framework for bioluminescence imaging center of mass-guided glioblastoma targeting

To cite this article: Behzad Rezaeifar *et al* 2022 *Phys. Med. Biol.* **67** 144003

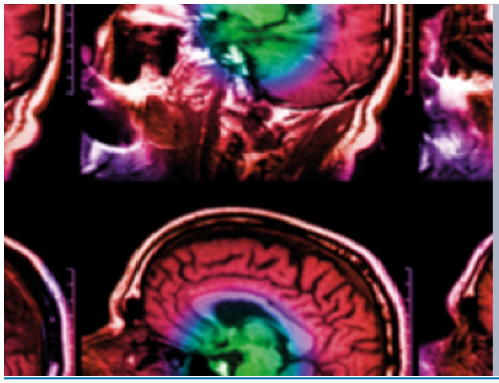

IOP Publishing Phys. Med. Biol. 67 (2022) 144003 https://doi.org/10.1088/1361-6560/ac79f8

Physics in Medicine & Biology

IPEM Institute of Physics and Engineering in Medicine

OPEN ACCESS

RECEIVED
30 September 2021

REVISED
2 May 2022

ACCEPTED FOR PUBLICATION
17 June 2022

PUBLISHED
8 July 2022

PAPER

A deep learning and Monte Carlo based framework for bioluminescence imaging center of mass-guided glioblastoma targeting

Behzad Rezaeifar[1,2], Cecile J A Wolfs[1], Natasja G Lieuwes[3], Rianne Biemans[3], Brigitte Reniers[2,4], Ludwig J Dubois[3,4] and Frank Verhaegen[1,4]

[1] Department of Radiation Oncology (Maastro), GROW—School for Oncology and Reproduction, Maastricht University Medical Centre+, Maastricht, The Netherlands
[2] Research group NuTeC, Centre for Environmental Sciences, Hasselt University, Diepenbeek, Belgium
[3] The M-Lab, Department of Precision Medicine, GROW—School for Oncology and Reproduction, Maastricht University, Maastricht, The Netherlands
[4] Senior authors with equal contribution.

E-mail: frank.verhaegen@maastro.nl

Keywords: small animal precision radiotherapy, bioluminescence tomography reconstruction, deep learning, 3D convolutional neural network, center of mass, transfer learning, Monte Carlo simulation

Supplementary material for this article is available online

Abstract

Objective. Bioluminescence imaging (BLI) is a valuable tool for non-invasive monitoring of glioblastoma multiforme (GBM) tumor-bearing small animals without incurring x-ray radiation burden. However, the use of this imaging modality is limited due to photon scattering and lack of spatial information. Attempts at reconstructing bioluminescence tomography (BLT) using mathematical models of light propagation show limited progress. *Approach.* This paper employed a different approach by using a deep convolutional neural network (CNN) to predict the tumor's center of mass (CoM). Transfer-learning with a sizeable artificial database is employed to facilitate the training process for, the much smaller, target database including Monte Carlo (MC) simulations of real orthotopic glioblastoma models. Predicted CoM was then used to estimate a BLI-based planning target volume (bPTV), by using the CoM as the center of a sphere, encompassing the tumor. The volume of the encompassing target sphere was estimated based on the total number of photons reaching the skin surface. *Main results.* Results show sub-millimeter accuracy for CoM prediction with a median error of 0.59 mm. The proposed method also provides promising performance for BLI-based tumor targeting with on average 94% of the tumor inside the bPTV while keeping the average healthy tissue coverage below 10%. *Significance.* This work introduced a framework for developing and using a CNN for targeted radiation studies for GBM based on BLI. The framework will enable biologists to use BLI as their main image-guidance tool to target GBM tumors in rat models, avoiding delivery of high x-ray imaging dose to the animals.

Introduction

In recent years, small animal image-guided irradiation platforms have boosted pre-clinical cancer research. These platforms ensure accurate treatment planning and dose delivery to animal models (Tillner *et al* 2014, Butterworth *et al* 2015, Koontz *et al* 2017, Verhaegen *et al* 2018). They often use integrated cone-beam computed tomography (CBCT) as their primary anatomical image guidance system. Due to limited soft-tissue contrast, often contrast-enhanced CBCT is needed to improve tumor segmentation accuracy. However, in some cases, such as glioblastoma multiforme (GBM), tumor visibility is low even with contrast agents. Furthermore, despite recent advances in precision imaging systems dedicated to small animals, current state-of-the-art systems deliver

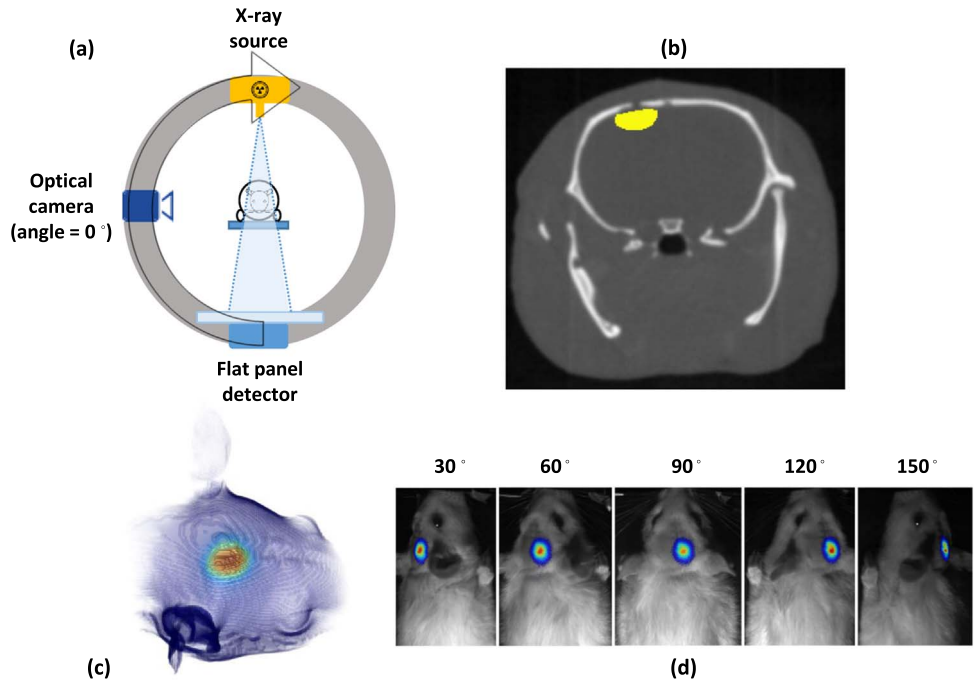

Figure 1. Small animal irradiation platform (XRad 225Cx, Precision X-ray, Inc.): (a) design of the integrated irradiation and imaging system (b) acquired micro-CBCT slice in an axial plane with hand-delineated tumor contour overlaid in yellow (c) surface rendering of Monte Carlo simulation of optical photons emerging from the skin (d) measured BLI signal at different angles, with the reference specified in (a), projected onto the optical light image.

a substantial imaging radiation dose to achieve the highest resolution required for targeting (Verhaegen *et al* 2011). There have been several attempts to reduce the delivered dose by using magnetic resonance (MR) guided treatment planning (Gutierrez *et al* 2015, Chiu *et al* 2018, Vanhove and Goethals 2019). However, since this technology is not yet integrated into modern pre-clinical irradiation platforms, CT-MR registration is required, which causes geometric uncertainties (Verhaegen *et al* 2018).

Bioluminescence imaging (BLI) can be a compelling option to facilitate image-guided radiotherapy. BLI relies on optical photons emitted by a chemical reaction between an enzyme and a corresponding injected substrate. In most *in vivo* BLI experiments, tumor cells are genetically modified to express firefly luciferase before implantation. Since these genetically modified cells are the only ones in the animal's body that generate such enzymes, only these cells emit light upon activation (Darne *et al* 2013). Therefore, hereafter the terms tumor and light source are used interchangeably.

BLI is performed by capturing the emitted photons outside the animal's body. Therefore, it can provide fast *in vivo* images with minimal background noise and no radiation dose. Currently, BLI is mainly used to acquire 2D projection images, possibly at several angles. Figure 1 shows a schematic representation of a small animal irradiation platform (XRad 225Cx, Precision X-ray, Inc., North Branford, CT) (Weersink *et al* 2014), an acquired slice of a CBCT volume, the result of Monte Carlo (MC) simulation of optical photons emerging from the skin, and the BLI observations. However, the lack of 3D spatial information, i.e. depth, shape and location, of the photon-emitting volume, as shown in figure 1(d), currently limits BLI use in small-animal preclinical cancer research. Thus, the development of accurate 3D bioluminescence tomography (BLT) reconstruction algorithms can open new doors for pre-clinical image-guided radiotherapy. In addition, BLT allows targeting selective regions inside tumors with ionizing radiation, investigating the tumor response to treatment, and many other research opportunities (O'Neill *et al* 2010, Kalra and Bally 2012). However, due to the limitations of the BLI-based targeting, a sub-millimeter targeting accuracy is considered satisfactory but there are no available guidelines or consensus about it.

Due to its importance in animal studies, much effort has been spent developing BLT reconstruction algorithms (Chaudhari *et al* 2005, Ahn *et al* 2008, Zhang *et al* 2016, Gao *et al* 2018, Zhang *et al* 2018, Deng *et al* 2020, Ren *et al* 2020). However, the reconstruction problem remains a challenge, and most of the commercial small-animal image-guided irradiators lack comprehensive BLT capabilities. Therefore, the development of novel methods to tackle this problem continues to be an active research area. We can categorize the current state-of-the-art methods into model-based (Deng *et al* 2020, Ren *et al* 2020) and deep learning (DL) based algorithms (Gao *et al* 2018).

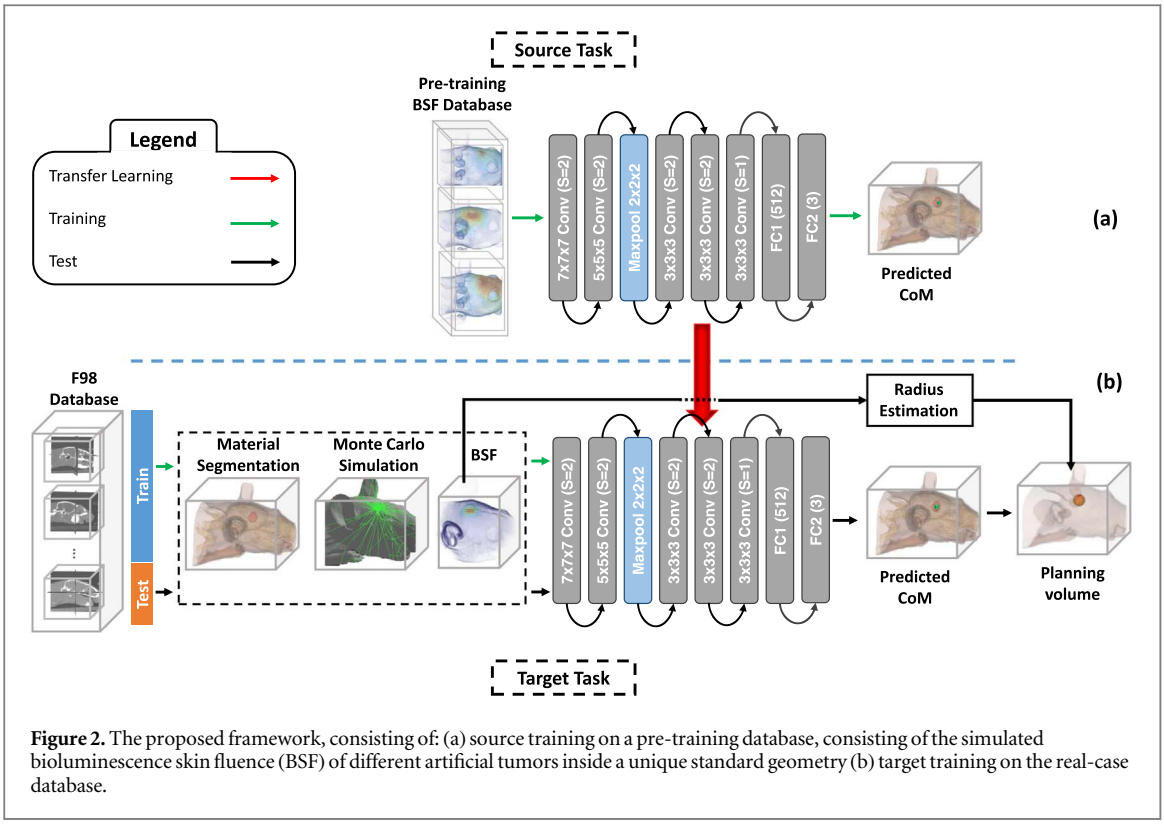

Figure 2. The proposed framework, consisting of: (a) source training on a pre-training database, consisting of the simulated bioluminescence skin fluence (BSF) of different artificial tumors inside a unique standard geometry (b) target training on the real-case database.

Model-based reconstruction methods aim to mathematically model light propagation inside the biological tissue and then solve the derived highly ill-posed inverse problem to reconstruct the 3D source distribution. These conventional methods require several estimations and approximations to solve the mathematical models that introduce errors in the final solution (Gao *et al* 2018). DL-based algorithms, on the other hand, utilize artificial intelligence (AI) to find the optimal solution and avoid modeling errors. It has been shown that AI can tackle many complicated inverse problems more efficiently than model-based counterparts (Vandewinckele *et al* 2020). To the best of our knowledge, the use of AI for BLT reconstruction has been limited to the work of Gao *et al* (2018). Gao's method consisted of registering all the possible inputs to a standard mesh, predicting the light source within the standard mesh, and then transferring back to the original space. However, the registration algorithm embedded within Gao's method can contribute considerably to the geometrical uncertainty. Furthermore, the multi-layer perceptron architecture used by Gao limits the maximum resolution or the depth of the DL algorithm that can be used.

This paper proposes a deep learning-based framework to improve BLT-guided radiation targeting for orthotopic GBM tumors. While Gao's method relies on registration, the proposed solution uses 3D photon counting at the skin boundary to predict the tumor's center of mass (CoM) and provides a unified solution for different geometries. The presented method employs deep convolutional neural networks (CNNs), allowing higher input resolution compared to Gao. In addition, the proposed deep-learning framework eliminates the necessity of image registration by employing transfer learning. Initially, a CNN is trained to predict the light source within a unique standard geometry. The acquired knowledge is then transferred to a second CNN to predict the light source in a variety of head geometries.

Materials and methods

The general framework, shown in figure 2, consists of three main steps: (1) Monte Carlo computation of 3D bioluminescence skin fluence (BSF) starting from optical photons emitted from a volume source embedded in the specimen, (2) predicting the center of mass (CoM) of the source volume using a CNN, and (3) defining the targeting volume based on the estimated tumor volume. Here, we consider the BSF as the number of optical photons emerging from the skin boundary. In *in vivo* experiments, BSF can be obtained using backprojection of the 2D BLI images recorded by the BLI camera onto the skin surface of the CBCT image (Weersink *et al* 2014). Currently, most BLI cameras only record under discrete angles, which results in a discrete sampling of the full BSF under specific angles. However, in this paper a continuous BSF is directly computed using Monte Carlo simulations, bypassing modeling the camera under various angles and the backprojection procedure. In addition, modelling of the optical camera would cause the simulations to be very slow and highly inefficient.

In this study, two sets of MC simulations of BSF are employed to create pre-training and real-case databases. The pre-training database contains a large number of tumor cases inside a reference geometry of one rat, while the real-case database includes the simulation output of several real rat GBM cases. By using the pre-training database, we allow a deep CNN to learn general features from observations inside a unique arbitrary geometry and then use transfer learning to generalize the acquired knowledge to a wide variety of rat head geometries. Subsequently, a regression model is used to estimate the tumor volume based on the input BSF. Then, assuming a spherical target volume, the predicted CoM and CBCT-based tumor volume can determine the target volume.

A total number of 57 labeled CBCT images are used in this study. This dataset is augmented to create the pre-training database containing 40 000 samples. The implementation details of the data augmentation algorithm is discussed in the supplementary materials B (available online at stacks.iop.org/PMB/67/144003/mmedia). The data within each database is split randomly into training, validation and test sets. Furthermore, 12-fold cross-validation is used to assess the deep learning model's performance on the real-case database. This means that the real-case database is split into twelve parts, and a model is trained on 11 parts and tested on the 12th part. This process is repeated for each of the 12 folds. This method is beneficial in evaluating small databases and allows the model to be trained and tested on all the samples in the database. Eventually, the quantified overlap between the predicted target volume and tumor volume will be considered as objective quality metric.

Monte Carlo simulations

In order to reconstruct the light source from the physical observations, i.e. 2D BLI images acquired with a camera, an accurate forward photon transport model is first needed. In this study, MC simulations with the GATE framework (Cuplov *et al* 2014) were employed as the forward model of light propagation to build the necessary databases. Four major assumptions were made prior to the simulations: (1) tumors are uniformly labeled with the light-emitting agents, (2) emission intensity is constant during the short imaging time, (3) the only materials in the region of interest are bone, brain, air, and water, and (4) light scattering and absorption is governed by constant scattering and absorption coefficients per material. The first two assumptions cause the simulations to have a constant number of emitted photons per unit volume, i.e. a voxel, while the latter two introduce simplification to the simulation geometry and the model.

The starting point of this study was previous *in vivo* experiments of an F98 rat orthotopic glioma model (Mowday *et al* 2020). Contrast-enhanced CBCT (CE-CBCT) images, with 0.1 mm resolution in all directions, were acquired at different time points in a tumor-growth study from 35 different animals resulting in 57 images in total. The brain hemispheres and tumor were carefully hand-delineated by trained specialists on each of these images. Hereafter, this database will be referred to as the F98 database.

All the images are padded or cropped into a single grid size of $375 \times 450 \times 375$, equal to the most common size in the database, providing a fixed size. Furthermore, the Hounsfield units (HU) are converted to mass density using the corresponding calibration curve, generated using a piecewise bi-linear fit between the mean HU and the mass density of specific materials in the calibration phantom (Vaniqui *et al* 2017). Subsequently, the simulation geometry is built by segmenting the mass density images into brain, water, air, and bone. The brain is considered as the hand-delineated contour. Bone and air contours are obtained by thresholding the mass density image with their corresponding thresholds. Everything else in the image is considered as water. Eventually, the geometry of the simulations is configured by assigning optical properties to different tissue segments. Figure 3 shows the reduced scattering (μ_s') and absorption coefficients (μ_a) of brain and bone tissues used in this study (Mesradi *et al* 2013, Soleimanzad *et al* 2017). In addition, the predefined optical properties in GATE are used for water and air. The optical source is defined based on the tumor contour with a similar emission spectrum as firefly luciferase (Zhao *et al* 2005) and the same optical properties as the brain tissue (figure 3). Finally, to decrease memory usage and simulation time, the resulting simulation geometry is downscaled to a $250 \times 300 \times 250$ grid with a resolution of 0.1551 mm^3.

Pre-training database

The pre-training database is constructed to include a large number of possible tumor variations inside a single reference geometry (i.e. a single rat specimen). Figure 4 displays the workflow used to build the pre-training database. Initially, one of the F98 samples, in which the region of interest is located in the center of the 3D volume and there is no bed present in the image, is chosen as the reference geometry. However, instead of directly simulating different tumor shapes and positions, an indirect approach, based on the superposition principle, is used in this study. In other words, the output of the MC simulation for any arbitrary tumor shape is represented by the sum of the outputs of independent simulations of smaller volume units within the tumor.

After obtaining the simulation geometry as described in the previous section, the brain is further partitioned into small voxel-like portions called super-voxels, as shown in figure 4. Each of the super-voxels includes several adjacent voxels grouped to decrease the total number of required simulations. Super-voxels are often cubical, except the super-voxels located at the edge of the brain. Subsequently, a MC simulation is done for every super-

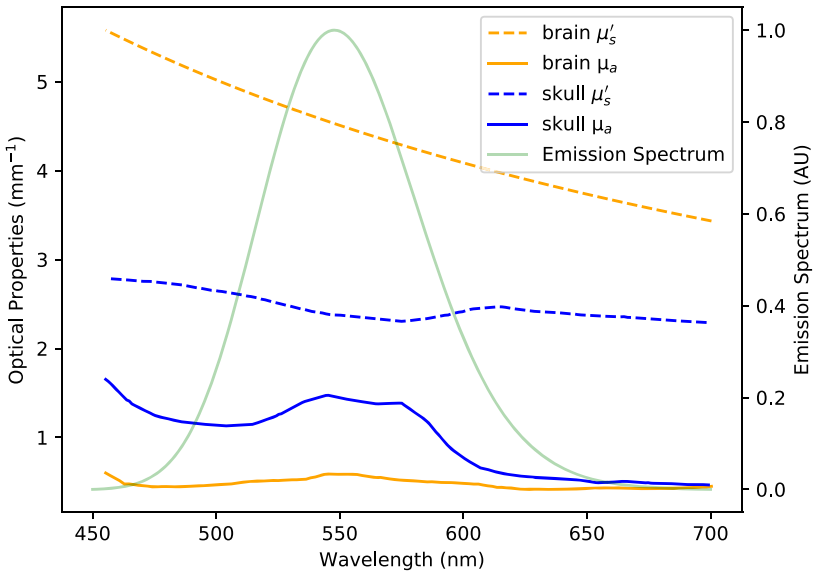

Figure 3. Optical properties spectrum of brain and bone, and photon emission spectrum used in the Monte Carlo simulations (Zhao *et al* 2005, Mesradi *et al* 2013, Soleimanzad *et al* 2017).

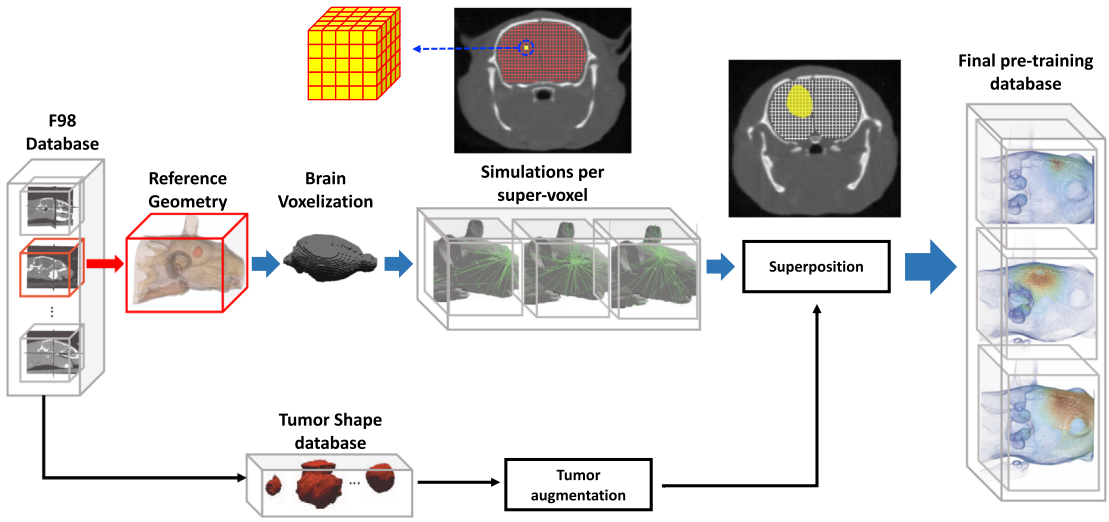

Figure 4. Workflow used to build the pre-training database.

voxel inside the brain, assuming that the super-voxel is the light source. Therefore, after repeating this procedure for every super-voxel inside the brain, the simulation output of any arbitrarily shaped tumor can be obtained by superposition of the output of the MC simulations for constituent super-voxels. However, there is always a trade-off between the number of available tumor cases covering all the possible shapes, based on the size of the super-voxels, and the computational cost. In other words, larger super-voxels limit the size and shape variety of the tumors quite drastically while reducing the number of MC simulations needed. In this study, the maximum size of the super-voxels is $5 \times 5 \times 5$ voxels, resulting in a minimum resolution of 0.77 mm^3 compared to the original resolution of 0.1551 mm^3.

The required simulations and consequently the simulation time for building the pre-training database are substantially reduced with the method described above. Nonetheless, the brain includes several hundred thousand voxels in a micro-resolution CBCT. Therefore, even with the super-voxel scheme, thousands of MC simulations are still needed to build the pre-training database. To decrease the computation time per simulation, we disabled the optical absorption process in the simulations for the pre-training database only, since tracking the many scattering interactions of photons which end up being absorbed before reaching the skin is highly inefficient. However, disabling absorption in the MC simulations causes errors in the BSF since a photon might reach places far away from the source, which it would not be able to reach in reality. Nevertheless, the pre-training

database serves to establish a crude relation between the geometry of the light source and the BSF, which will then in subsequent steps be refined.

Once the BSF is known for every super-voxel, a realistic database of tumor cases is needed to build the pre-training database. In this study, the hand-delineated tumor contours of the F98 database are used as the possible tumor shapes. The tumor shape database is further augmented by applying semi-random affine transformations, with zero translation, to the initial shapes. The augmentation algorithm is designed semi-randomly to ensure that all the real shapes, with exact scale and orientation, are present in the final database, as well as a large population of random cases. Then, for each case in the augmented shape database, a vector of all the possible coordinates for the tumor's central placement is calculated, where the entire tumor is encapsulated inside the brain. The final pre-training database consists of the tumor cases that resulted from random sampling of the coordinate vector. This way, we increased the size of the pre-training database drastically to more than 40 000 cases. Finally, the MC-simulated BSF is obtained for each of these cases by combining the simulation output corresponding to super-voxels inside the tumor.

Real case simulations

In the second database, hereafter referred to as real-case database, one MC simulation is performed for each of the samples in the F98 animal experiment. In contrast to the pre-training database, one simulation geometry is constructed for each animal, based on their respective CE-CBCT head volume, as described before. In addition, the light source is considered as the hand-delineated tumor contour. Furthermore, the photon absorption process is modelled in the MC simulations for this database to better fit the actual measurements.

CNN-based center of mass predictor

This study uses a 3D CNN consisting of five convolutional layers, one max-pooling layer, and two fully connected layers to predict the tumor's CoM (figure 2). The network's input consists of the normalized 3D BSF at the skin level, and the output is the set of 3D coordinates of the tumor's CoM. Input normalization is performed by rescaling the values of 3D BSF within the range [0, 1]. The hyperparameters of the network are optimized by a manual grid search using the pre-training database. Furthermore, an on-the-fly data augmentation algorithm, consisting of rigid-body transformation, is implemented for the real-case training phase to increase model robustness and generalizability. The aforementioned transformation includes small random rotations around the sagittal axis and translation since the prone animal is supported by a bed and an anesthesia nose cone. In addition to data augmentation, we included additive Gaussian noise in the on-the-fly data augmentation algorithm to make the model more robust against realistic measurement noise.

As shown in figure 5, the training process consists of the following steps: (i) collection of pre-processing steps including normalization and on-the-fly augmentation, (ii) applying the current state of the CNN model to the data and predicting the CoM, (iii) comparing the predicted CoM with the ground truth based on a loss function and (iv) adjusting the parameters of the CNN model to minimize to the error. In this paper, we used the mean squared error (MSE) as the loss function determining the error between the predictions and the ground truth. Furthermore, an early stopping criterion based on the best validation loss is implemented to avoid possible overfitting.

The proposed framework utilizes transfer learning to improve the learning procedure. Transfer learning consists of first training a model on a general large database and then fine-tuning that model for a specific task (Pan and Yang 2010). As a result, the pre-trained model learns the most important features from a sufficiently meaningful database and fine-tunes the learned knowledge to fit best to the target problem. Romero *et al* (2020) showed transfer learning is beneficial in cases with small-size training database, only if the pre-training corresponds to the same anatomical site as the target problem. In other words, the similarity between pre-training and the target databases can impact the performance of the deep-learning model. Therefore, in this study, both pre-training and real-case databases are built using MC simulations, thus ensuring the similarity between source and target task. However, there are still two major differences: (1) the pre-training database consists of various tumor shapes inside a unique head geometry while this is not the case for the real-case database, and (2) MC simulation in the pre-training database is done without considering optical photon absorption. Subsequently, any solution on the source domain cannot achieve high performance when directly applied on the target domain. Therefore, weights trained during the pre-training are transferred to a new identical model as the initial weights. This process is known as transfer learning (Pan and Yang 2010) and is often used to overcome issues caused by small-sized training database in the target task. As a result, the new model can employ the acquired prior knowledge in the context of the target problem. Consequently, all the transferred weights are re-trained using the real-case database to yield the best result. Further details about the implementation of the transfer learning algorithm used in this paper are provided in the supplementary material, section C.

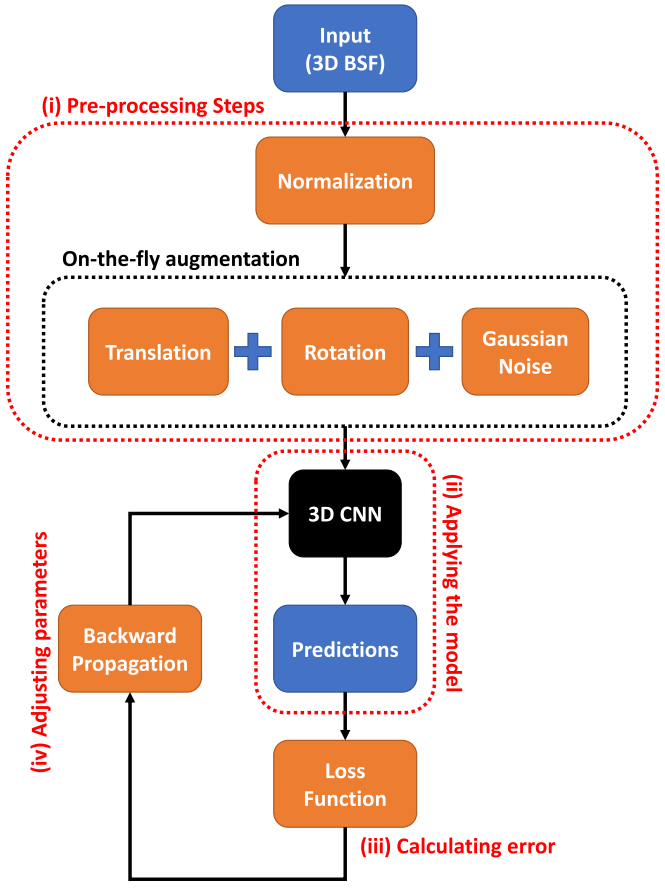

Figure 5. Details of the training process: 3D bioluminescence skin fluence (BSF) is used as input for the network after pre-processing steps and the parameters of the network are adjusted based on the loss function, i.e. mean square error.

Targeting planning volume

In this study, the hand-delineated CBCT-based tumor contours are considered the ground truth for the gross tumor volume (GTV). The GTV is further simplified and approximated as the enclosing sphere containing the tumor since almost all commercially available small animal irradiators currently lack the capability to shape complex radiation fields and offer mostly circular or rectangular fields (Verhaegen *et al* 2018). Furthermore, tumors are typically irradiated with substantial geometric margins to avoid tumor miss and take tumor motion and setup uncertainties into account (Vaniqui *et al* 2019). Therefore, we can estimate the BLI-based GTV (bGTV) and build the corresponding planning target volume (PTV) with the predicted tumor's CoM and volume. Tumor cells are the only bioluminescence light emitter inside the animal resulting in an almost zero background signal. Thus, the total number of detected photons correlates linearly with the tumor volume (Deng *et al* 2020, Mowday *et al* 2020). Therefore, tumor volume can be estimated by performing logistic regression between the total number of surface photon counts and the tumor volume in the training database.

Once the BLI-based gross tumor volume (bGTV) is obtained, a sphere around the predicted CoM is considered as the bioluminescence-based PTV (bPTV). The radius of the bPTV is calculated based on equation (1)

$$R = \sqrt[3]{\frac{3}{4\pi} bGTV} + m, \tag{1}$$

where $bGTV$ is the bioluminescence-based gross tumor volume and m is a constant margin. Here, the sum of the average CoM and volume prediction uncertainties is considered as the margin (equation (2)).

$$m = u_{CoM} + u_{volume}. \tag{2}$$

This study uses two metrics to evaluate the predicted bPTV, namely tumor and healthy tissue coverage. We defined the coverage metric for the tissue of interest as follows:

$$C_{tissue} = \frac{V_{tissue}^{bPTV}}{V_{tissue}^{total}}, \tag{3}$$

where V_{tissue}^{bPTV} and V_{tissue}^{total} correspond to the number of voxels inside the predicted planning volume and the total number of voxels for each specific tissue. In an ideal case, the algorithm should score 0% healthy tissue coverage while targeting all of the tumor. However, this is not feasible due to the spherical approximation of the tumor shape.

In order to underline the inherent uncertainties of the proposed method and their contribution to the targeting accuracy, the coverage metrics are employed in four different scenarios: (a) the ideal case in which both CoM and tumor volume are estimated perfectly with zero error, namely GT1, (b) the situation where the CoM is perfectly captured but the tumor volume is estimated according to the proposed solution, GT2, (c) the case in which the volume is predicted accurately with no error but CoM is predicted using the CNN network, referred as GT3, and (d) both CoM and volume are predicted according to the presented solution. Furthermore, the three ideal cases, namely GT1-3, do not contain any added margin ($m = 0$) to allow a fair investigation of each uncertainty source in the proposed framework and show the effect of added margin. Consequently, separating the effect of each prediction uncertainty provides a better understanding of the proposed method and its limitations.

Results

The performance of the proposed method is evaluated in two parts: (1) CoM prediction accuracy and (2) planning coverage evaluations. For the former, we investigated the CoM predictions using the ΔCoM metric, which measures the Euclidean distance in millimeter between the CT-based and predicted CoM. For the latter, tumor and healthy tissue coverage metrics are obtained, which quantify which percentage of each tissue falls inside the planning volume (equations (2), (3)). This section describes all the objective measures with the median, interquartile range, and outliers.

The proposed method provided excellent performance in ΔCoM. As shown in figure 6, the proposed method can achieve submillimeter accuracy in CoM predictions in both databases. The median ΔCoM in the pre-training database is around 0.1 mm with an interquartile range of 0.12 mm which is of the same order as the image slice thickness in the CT image (0.1 mm). The method's performance decreased when moving to the real-case database with a median and interquartile range of 0.6 ± 0.43 mm with only one outlier of 1.5 mm, corresponding to a 1 mm^3 tumor. Figures 6(b) and (c) show the variation of ΔCoM based on the tumor volume in each database. As shown in figure 6(b), the proposed method can provide accurate results for various tumor sizes and in most cases the predicted CoM falls within the boundaries of the tumor. However, the model struggles to predict the CoM for very small tumors, with a volume smaller than 10 mm^3 (about 2700 image voxels), since the resulting BSF is relatively small and susceptible to noise. In practice, targeting tumors below 10 mm^3 is very challenging because it would require beams of approximately 1–3 mm. If we exclude the results of this category of tumors, the model performance improves to 0.5 ± 0.4 mm. In addition to accurate predictions, DL models can provide fast inference. The proposed network's average prediction time is 18.87 ± 0.04 ms on an NVIDIA Quadro RTX 5000 GPU (Santa Clara, CA, USA).

Figure 7 underlines the importance of transfer learning with the pre-training database in the proposed framework. In this figure, two models have been trained with an identical training database: one is a raw model with randomly initialized weights and the other model is the result of pre-training. These two models are referred to as model without and with transfer learning in figure 6. As shown, the training loss, i.e. the mean squared error between predicted and actual CoM in the training phase, starts at a much lower point and converges better to the end point. Therefore, the model with transfer learning is far more capable in learning and converging towards a better solution.

The performance evaluation of the bPTV is shown in figure 8, with a linear fit of CT-based GTV versus the total BSF shown in supplementary materials (Pearson's rvalue of 0.8). bPTV estimation based on the predicted CoM shows promising results. The proposed method averages more than $94 \pm 9\%$ tumor coverage while keeping the mean healthy tissue coverage around $7 \pm 3\%$.

Finally, figure 9 presents the visualization of the BLI-based tumor targeting as elaborated in this paper. As can be observed, the proposed method provides good overlap of the targeting volume with the tumor while sparing most of the healthy tissue.

Results of the uncertainty analysis of the proposed solution are presented in figure 10. The first ground-truth case (GT1) targets only 79% of the tumor with maximum healthy tissue conservation, with an average brain coverage of 0.5%. In the second ideal case (GT2), both metrics on average increased to 84% and 0.9%. Finally, the third ideal scenario (GT3) resulted in a substantial decrease in the tumor coverage with an average of 49.3% while further increasing the average brain coverage to 1%.

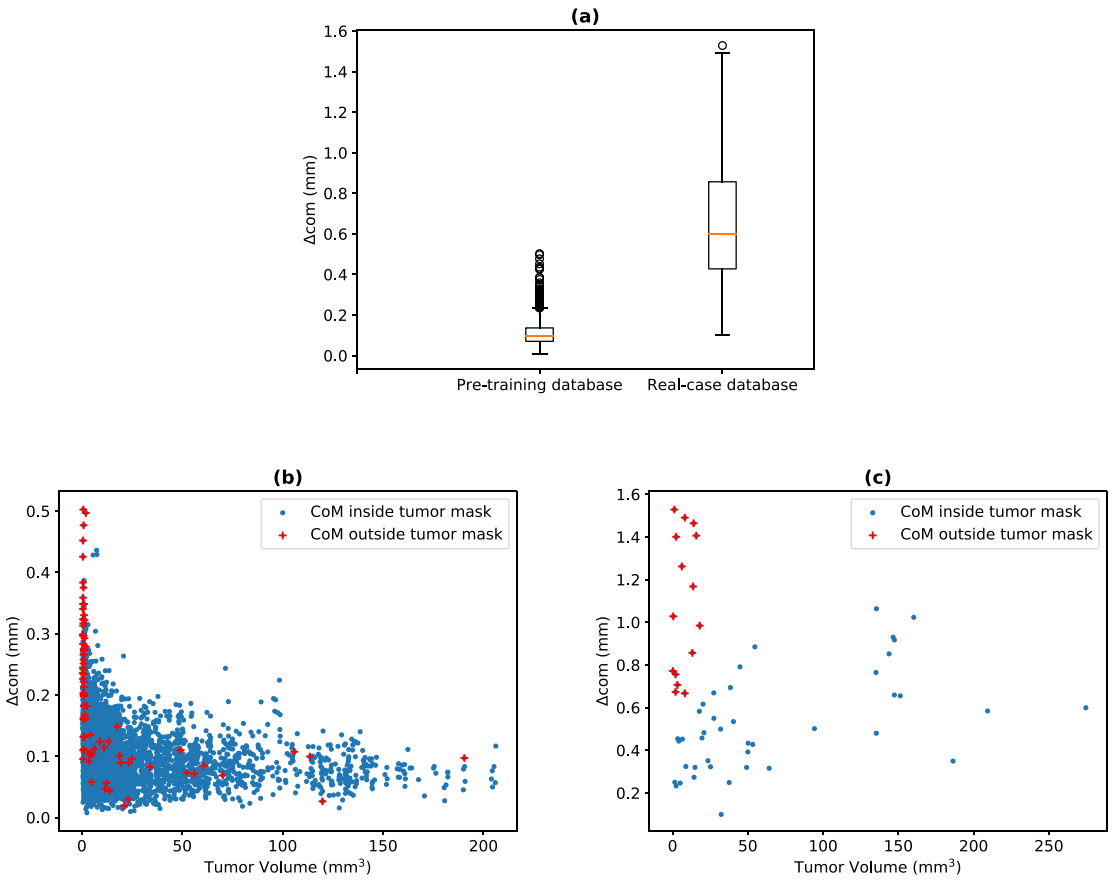

Figure 6. Performance evaluation of the proposed method in CoM prediction: (a) comparison of model performance in pre-training and real-case database (b) scatter plot of ΔCOM versus tumor volume in pre-training database (c) scatter plot of ΔCOM versus tumor volume real-case database.

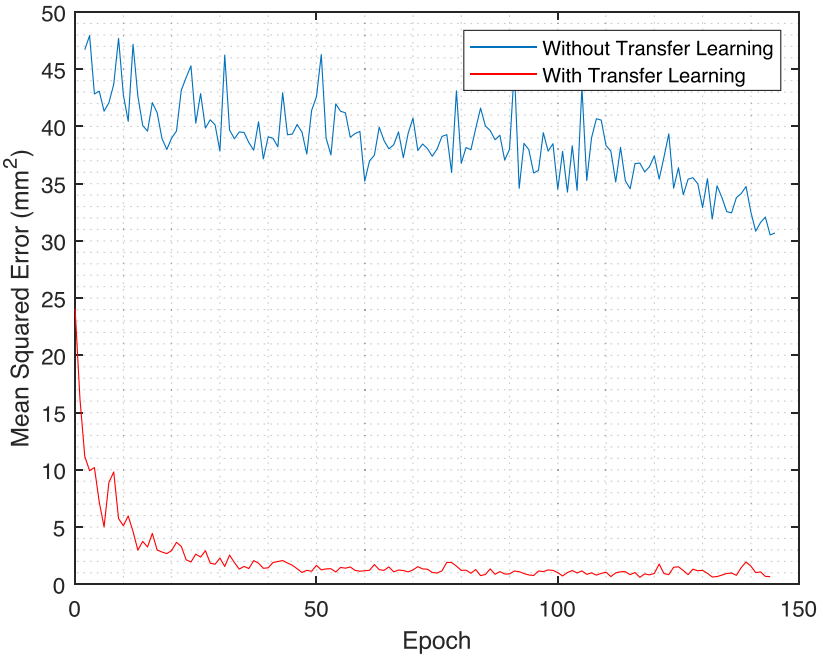

Figure 7. Effect of transfer learning on the training process: progression of training loss of the first 150 epochs for a network without transfer learning (blue) and the same network with transfer learning (red).

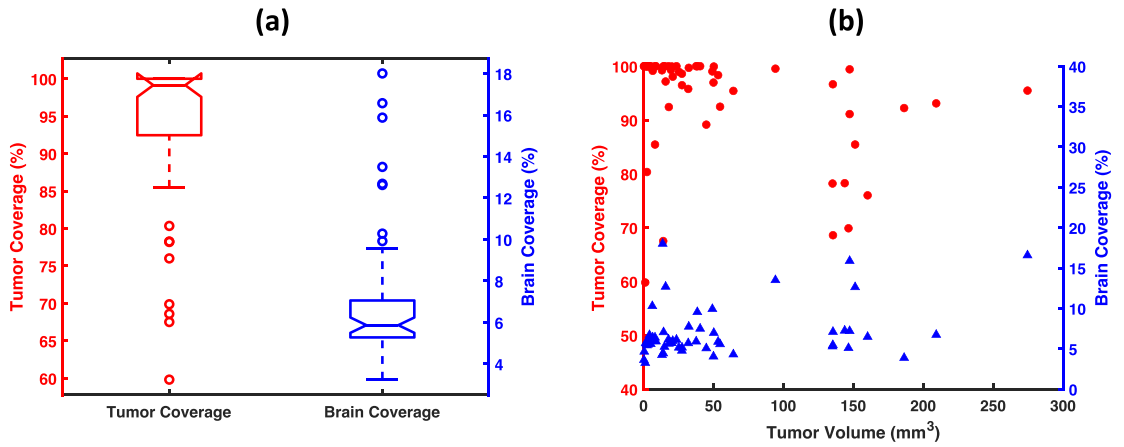

Figure 8. Performance evaluation of tissue coverage: (a) boxplot of coverage of tumors (red) and normal tissue (blue) (b) effect of tumor volume on both tissue coverages.

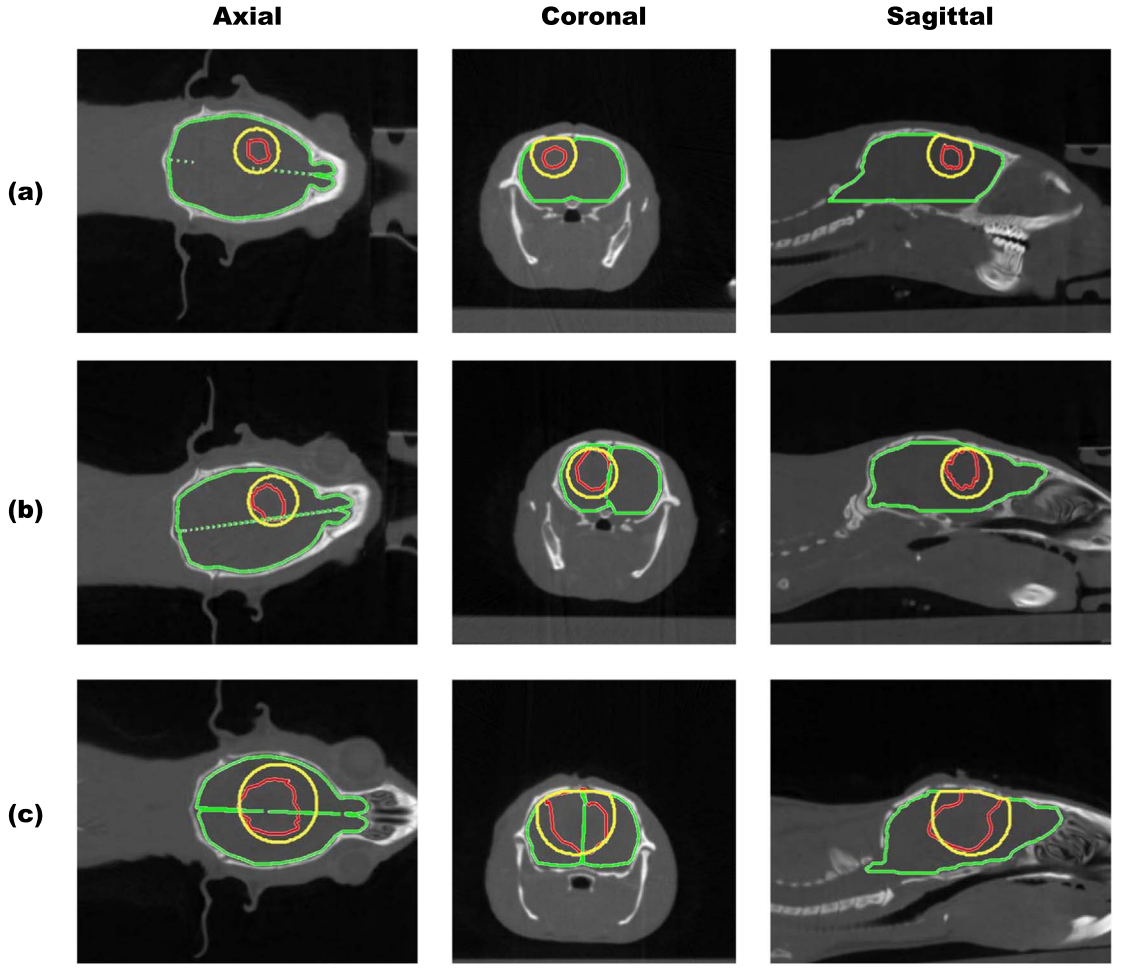

Figure 9. Visualizations of the output in three different animals (a)–(c) shown in different planes. Green, red, and yellow contours represent brain, tumor and predicted BLI-based targeting volume respectively.

Discussion

This paper proposed a deep CNN to predict the tumor's CoM based on BLI and estimate the treatment volume accordingly. Nearly all previously published methods rely on very complicated and approximative mathematical physics models of light propagation to predict light distribution within the biological tissue as a surrogate for tumor location. Solving these models needs various approximations and estimations, which can reduce the

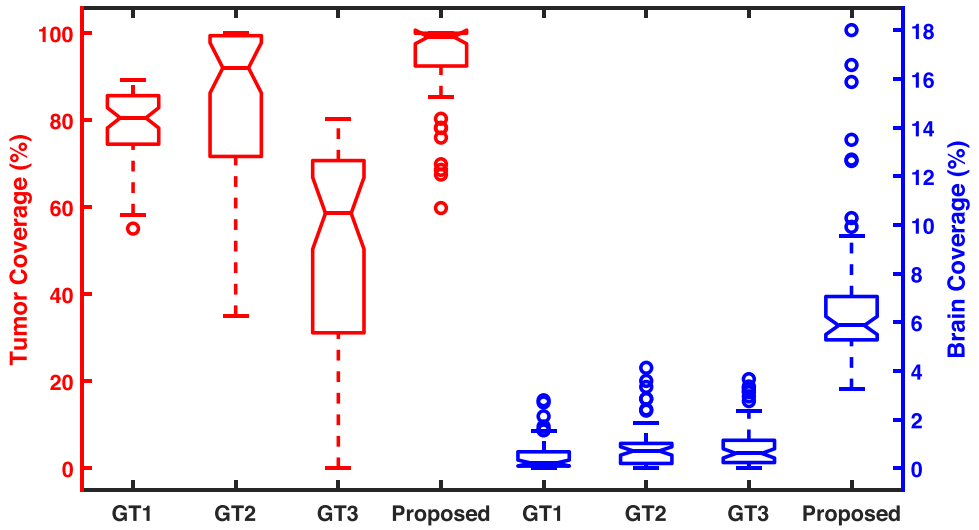

Figure 10. The performance of the proposed method in four different scenarios: (GT1) both CoM and tumor volume are estimated ideally equal to the ground truth, (GT2) CoM is predicted accurately but volume is estimated according to the proposed framework, (GT3) volume estimation is accurate while CoM is predicted using the deep learning model, and the result of the proposed solution as presented in figure 8.

reconstruction accuracy. In contrast, AI algorithms can learn the best statistical model that can be fitted to the data. Although often slow during the training process, AI solutions can be fast during the inference phase. The proposed method achieves a runtime of milliseconds in the inference phase and it can thus contribute substantially to real-time targeting once translated to real BLI measurements. Furthermore, the proposed solution can predict the location of the tumor with sub-millimeter accuracy and construct a spherical target volume that captures, on average, more than 94% of the tumor while only including 7% of the brain volume, all of which provide an accurate BLI-based GBM targeting for rat models.

In this study, we only investigated the feasibility of using a CNN to improve the reconstruction accuracy of BLI determined volumes. The proposed method can achieve high accuracy in predicting tumor location and encompassing volume in the reference geometry. In the pre-training database, the accuracy of the position prediction is approximately equal to the CBCT imaging resolution used to create the inputs. However, training one model for each unique animal is a cumbersome task. Therefore, we explored transfer learning to solve this issue and extrapolate the learned knowledge to predict CoM in different animals. Figure 6 highlights the added value of transfer learning. Although we noticed a slight increase in the ΔCoM in the real-case database compared to the pre-training, the final result still provides sub-millimeter accuracy in most cases.

Since designing complex field shaping devices for small animal irradiation platforms is a very challenging task, all commercial units use static collimators with circular or rectangular shapes to irradiate the planned volume. Therefore, in this study, the BLI-based gross target volume was estimated using a sphere around the predicted CoM. As shown in figure 7, the bPTV covers 94% of the tumor on average and spares most of the normal tissue around it. Therefore, the proposed algorithm can be used to provide bioluminescence-based targeting for a large variety of cases. However, in this paper, only simulated BSF and not camera-acquired BSF of real-case GBM bioluminescence acquisitions are used, as the first step towards developing a CNN-based method for BLI-based targeting. However, approximating the target volume as an enveloping sphere brings inherent error to the proposed solution, which is shown in figure 10. In the best-case scenario, for which both CoM and the volume are known, employing the enveloping sphere approximation will reduce the tumor coverage score substantially. However, this effect can be mitigated by adding a margin to the spherical envelope. Furthermore, it has been confirmed that the volume estimation is overestimating the size of the tumor in most cases. However, the inaccuracy imposed by estimating tumors with their enveloping sphere, even in the best-case scenario, limits the overall accuracy of the model. In the future, more advanced AI models can be employed to enhance the proposed framework and enable full tumor shape prediction. In addition to the inherent limitations of the spherical estimation method used here, the uncertainties incorporated in CoM and volume predictions, as presented in figure 10, contribute to increased brain coverage while reducing tumor coverage. However, the added margin compensates for such errors and provides an acceptable tumor coverage while keeping the brain coverage below 10%.

In reality, BSF cannot be measured directly and it should be reconstructed using a limited set of projections captured by the camera. This, in the best case, can only generate a partial indirect measurement of the actual BSF.

In the future, the proposed framework of this paper will be adopted for real measurements and the accuracy of the model will be further improved by adding more training samples to the database.

The presented CNN-based framework can achieve deeper layers in limited memory compared to the fully connected multi-layered perceptron (MLP) counterpart implemented by Gao *et al* (2018). Therefore, CNN-based models can extract and learn more features in the same amount of memory. In addition, Gao's model relies on registration between a standard mesh and the input mesh, which brings additional computational cost and uncertainty. Deng *et al* (2020) present a CoM prediction algorithm with comparable accuracy to this paper's CNN-based framework. While both Deng's method and the method presented in this work are based on a combination of CoM and volume predictions to target tumors, Deng's method relies on mathematical models of light propagation and a measured unirradiated tumor growth curve. Comparison of the reported results, between the CNN-based and Deng's method, shows the superior performance of the CNN-based method. While Deng *et al* achieved an average of 1 mm ΔCoM, the proposed CNN-based method can result in 0.6 mm ΔCoM on average. However, the observed improvement in the presented CNN-based method can be linked to the use of idealized cases, i.e. MC simulations, in this study. Nonetheless, a drawback of Deng's method is its dependence on the unirradiated tumor growth curve. Considering the purpose of BLI-based targeting, tumors will likely respond to the treatment which slows their growth and puts the reliability of tumor growth curve into question. Consequently, their proposed algorithm cannot be employed in fractionated radiation studies. The presented method, on the other hand, does not rely on the tumor growth curve and can be a useful tool in small animal GBM studies.

The proposed CNN architecture imposes a limitation on the general use of the developed method. In other words, the predicted single-coordinate CoM limits the valueability of the proposed framework for metastatic tumors where two or more clusters of tumor cells or formed. However, the studied rat GBM model is not a metastatic tumor model and only forms a single compact tumor upon proper implantation. To address this limitation, in future works image-to-image transformer networks such as U-Net and autoencoders can be utilized.

The findings of this paper should be extended and validated in in-phantom and *in vivo* animal studies. Thus longitudinal BLI imaging can replace longitudinal CE-CBCT imaging, delivering no imaging dose to the animals. Furthermore, the presented framework can be extended using more sophisticated deep-learning models, such as generative adversarial networks (GANs), to obtain the BLI-based tumor contour. This would allow for even more accurate targeting and facilitates animal studies even further. In addition, continuous bioluminescence imaging in contrast to imaging at discrete angles might add value to the reconstruction algorithms. However, measurement noise due to hardware limitations might be a bottleneck in such an approach.

Conclusion

In this paper, we developed a framework using deep learning for bioluminescence-based targeting for GBM animal models. The proposed model can predict the tumor's CoM with submillimeter accuracy, except for tumors smaller than 10 mm^3. In addition, we showed that the accuracy of the proposed planning scheme with circular encompassing fields is sufficient for targeting with a high average tumor coverage. Our findings can open the door to further investigation of AI-based approaches in the field of bioluminescence tomography. This paper's findings can help biologists investigate GBM using bioluminescence markers. CNN based BLI targeting may also reduce the planning time compared to physics model-based counterparts. However, this paper mainly focused on developing the framework based on Monte Carlo simulations to generate the necessary training database. Further studies are needed to extend the framework for real BLI measurements.

Acknowledgments

The authors would like to thank Dr Brent van der Heyden for fruitful discussion. This work was partially supported by special research fund for double doctorate degree projects in the framework of the cooperation between Hasselt university and Maastricht UMC + (Grant No. BOF17DOCMA13).

Ethical statement

μCBCT images were re-used from previous animal experiments, which were all in accordance with local institutional guidelines for animal welfare and approved by the Animal Ethical Committee of Maastricht University (protocol number 2017-012).

ORCID iDs

Behzad Rezaeifar https://orcid.org/0000-0002-2125-1154
Cecile J A Wolfs https://orcid.org/0000-0001-6428-2762
Brigitte Reniers https://orcid.org/0000-0001-7084-4696
Ludwig J Dubois https://orcid.org/0000-0002-8887-4137
Frank Verhaegen https://orcid.org/0000-0001-8470-386X

References

Ahn S, Chaudhari A J, Darvas F, Bouman C A and Leahy R M 2008 Fast iterative image reconstruction methods for fully 3D multispectral bioluminescence tomography *Phys. Med. Biol.* **53** 3921–42

Butterworth K T, Prise K M and Verhaegen F 2015 Small animal image-guided radiotherapy: status, considerations and potential for translational impact *Br. J. Radiol.* **88** 20140634

Chaudhari A J, Darvas F, Bading J R, Moats R A, Conti P S, Smith D J, Cherry S R and Leahy R M 2005 Hyperspectral and multispectral bioluminescence optical tomography for small animal imaging *Phys. Med. Biol.* **50** 5421–41

Chiu T D, Arai T J, Campbell Iii J, Jiang S B, Mason R P and Stojadinovic S 2018 MR-CBCT image-guided system for radiotherapy of orthotopic rat prostate tumors *PLoS One* **13** e0198065

Cuplov V, Buvat I, Pain F and Jan S 2014 Extension of the GATE Monte-Carlo simulation package to model bioluminescence and fluorescence imaging *J. Biomed. Opt.* **19** 026004

Darne C, Lu Y and Sevick-Muraca E M 2013 Small animal fluorescence and bioluminescence tomography: a review of approaches, algorithms and technology update *Phys. Med. Biol.* **59** R1–64

Deng Z *et al* 2020 *In vivo* bioluminescence tomography center of mass-guided conformal irradiation *Int. J. Radiat. Oncol.***Biol.***Phys.* **106** 612–20

Gao Y, Wang K, An Y, Jiang S, Meng H and Tian J 2018 Nonmodel-based bioluminescence tomography using a machine-learning reconstruction strategy *Optica* **5** 1451–4

Gutierrez S, Descamps B and Vanhove C 2015 MRI-only based radiotherapy treatment planning for the rat brain on a small animal radiation research platform (SARRP) *PLoS One* **10** e0143821

Kalra J and Bally M 2012 Bioluminescence applications in preclinical *Bioluminescence - Recent Advances in Oceanic Measurements and Laboratory Applications* ed D Lapota (London: IntechOpen) (https://doi.org/10.5772/36736)

Koontz B F, Verhaegen F and De Ruysscher D 2017 Tumour and normal tissue radiobiology in mouse models: how close are mice to mini-humans? *Br. J. Radiol.* **90** 20160441

Mesradi M, Genoux A, Cuplov V, Abi Haidar D, Jan S, Buvat I and Pain F 2013 Experimental and analytical comparative study of optical coefficient of fresh and frozen rat tissues *J. Biomed. Opt.* **18** 117010

Mowday A M, Lieuwes N G, Biemans R, Marcus D, Rezaeifar B, Reniers B, Verhaegen F, Theys J and Dubois L J 2020 Use of a luciferase-expressing orthotopic rat brain tumor model to optimize a targeted irradiation strategy for efficacy testing with temozolomide *Cancers* **12** 1585

O'Neill K, Lyons S K, Gallagher W M, Curran K M and Byrne A T 2010 Bioluminescent imaging: a critical tool in pre-clinical oncology research *J. Pathol.* **220** 317–27

Pan S J and Yang Q 2010 A survey on transfer learning *IEEE Trans. Knowl. Data Eng.* **22** 1345–59

Ren S, Wang L, Zeng Q, Chen D, Chen X and Liang J 2020 Effective reconstruction of bioluminescence tomography based on GPU-accelerated inverse Monte Carlo method *AIP Adv.* **10** 105329

Romero M, Interian Y, Solberg T and Valdes G 2020 Targeted transfer learning to improve performance in small medical physics datasets *Med. Phys.* **47** 6246–56

Soleimanzad H, Gurden H and Pain F 2017 Optical properties of mice skull bone in the 455- to 705-nm range *J. Biomed. Opt.* **22** 010503

Tillner F, Thute P, Bütof R, Krause M and Enghardt W 2014 Pre-clinical research in small animals using radiotherapy technology—a bidirectional translational approach *Z. Med. Phys.* **24** 335–51

Vandewinckele L, Claessens M, Dinkla A, Brouwer C, Crijns W, Verellen D and Van Elmpt W 2020 Overview of artificial intelligence-based applications in radiotherapy: Recommendations for implementation and quality assurance *Radiother. Oncol.* **153** 55–66

Vanhove C and Goethals I 2019 Magnetic resonance imaging-guided radiation therapy using animal models of glioblastoma *Br. J. Radiol.* **92** 20180713

Vaniqui A, Van Der Heyden B, Almeida I P, Schyns L E, Van Hoof S J and Verhaegen F 2019 On the determination of planning target margins due to motion for mice lung tumours using a four-dimensional MOBY phantom *Br. J. Radiol.* **92** 20180445

Vaniqui A, Schyns L E J R, Almeida I P, Van Der Heyden B, Van Hoof S J and Verhaegen F 2017 The impact of dual energy CT imaging on dose calculations for pre-clinical studies *Radiat. Oncol.* **12** 181

Verhaegen F *et al* 2018 ESTRO ACROP: Technology for precision small animal radiotherapy research: Optimal use and challenges *Radiother. Oncol.* **126** 471–8

Verhaegen F, Granton P and Tryggestad E 2011 Small animal radiotherapy research platforms *Phys. Med. Biol.* **56** R55–83

Weersink R A, Ansell S, Wang A, Wilson G, Shah D, Lindsay P E and Jaffray D A 2014 Integration of optical imaging with a small animal irradiator *Med. Phys.* **41** 102701

Zhang B, Wang K K-H, Yu J, Eslami S, Iordachita I, Reyes J, Malek R, Tran P T, Patterson M S and Wong J W 2016 Bioluminescence tomography-guided radiation therapy for preclinical research *Int. J. Radiat. Oncol., Biol., Phys.* **94** 1144–53

Zhang B, Yin W, Liu H, Cao X and Wang H 2018 Bioluminescence tomography with structural information estimated via statistical mouse atlas registration *Biomed. Opt. Express* **9** 3544–58

Zhao H, Doyle T, Coquoz O, Kalish F, Rice B and Contag C 2005 Emission spectra of bioluminescent reporters and interaction with mammalian tissue determine the sensitivity of detection *in vivo J. Biomed. Opt.* **10** 041210